

**Electrocatalytic Nitrate Reduction on Rhodium Sulfide
Compared to Pt and Rh in the Presence of Chloride**

Journal:	<i>Catalysis Science & Technology</i>
Manuscript ID	CY-ART-07-2021-001369.R1
Article Type:	Paper
Date Submitted by the Author:	16-Sep-2021
Complete List of Authors:	Richards, Danielle; University of Michigan Young, Samuel; University of Michigan, Chemical Engineering Goldsmith, Bryan; University of Michigan, Chemical Engineering Singh, Nirala; University of Michigan, Chemical Engineering

Electrocatalytic Nitrate Reduction on Rhodium Sulfide Compared to Pt and Rh in the Presence of Chloride

Danielle Richards,^{a,b} Samuel D. Young,^{a,b} Bryan R. Goldsmith,^{a,b,*} Nirala Singh^{a,b,*}

^a Department of Chemical Engineering, University of Michigan, Ann Arbor, MI 48109-2136, USA

^b Catalysis Science and Technology Institute, University of Michigan, Ann Arbor, MI 48109-2136, USA

* Corresponding authors: bgoldsm@umich.edu, snirala@umich.edu

ABSTRACT: Chloride poisoning is a serious problem for the electrocatalytic reduction of aqueous nitrate (NO_3^-) and improved electrocatalysts are needed. Here we study the electrocatalytic activity of rhodium sulfide supported on carbon ($\text{Rh}_x\text{S}_y/\text{C}$) for the reduction of nitrate and compare it against Pt/C and Rh/C in the presence of chloride. Between 0.05–0.15 V vs. RHE, $\text{Rh}_x\text{S}_y/\text{C}$ has a steady-state nitrate reduction current density in 1 M H_2SO_4 + 1 M NaNO_3 that is 1.6–5.6 times greater than Rh/C (the most active metal electrocatalyst) and 10–24 times greater than Pt/C. Current densities are decreased by 37% for $\text{Rh}_x\text{S}_y/\text{C}$, 62% for Rh/C, and 40% for Pt/C at 0.1 V vs. RHE in the presence of 1 mM chloride. The decrease in nitrate reduction activity for Pt, Rh, and Rh_xS_y is due to the competitive adsorption of chloride and nitrate on the surface. Density functional theory (DFT) modeling predicts that chloride poisoning will persistently inhibit nitrate reduction on metals due to linear adsorbate scaling relations between nitrate and chloride. DFT calculations and microkinetic modeling of our experimental measurements predict that nitrate converts to nitrite via an H-assisted dissociation mechanism on Pt and direct nitrate dissociation on Rh and Rh_xS_y . Pristine Rh_xS_y (i.e., Rh_3S_4 , Rh_2S_3 , and $\text{Rh}_{17}\text{S}_{15}$) terraces are predicted to be inactive toward nitrate reduction. In contrast, sulfur vacancies in Rh_3S_4 terraces are predicted to be active for nitrate reduction, but also bind chloride strongly. Thus, sulfur-defected Rh_3S_4 rationalize the experimentally observed high activity but moderate chloride poison-resistance of $\text{Rh}_x\text{S}_y/\text{C}$ for nitrate reduction.

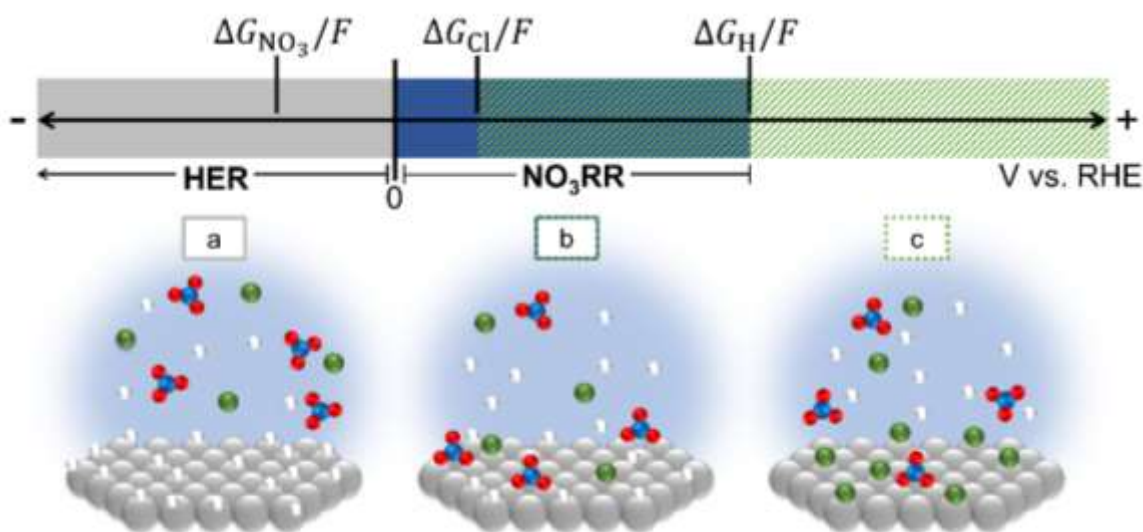
Key Words: nitrogen cycle, electrocatalytic water treatment, catalyst poisoning, metal sulfides, density functional theory modeling

1. INTRODUCTION

Nitrate (NO_3^-) contamination of lakes, rivers, and ground water from agricultural, livestock, and industrial activities is a major threat to human (e.g., congenital disease, cancer) and ecosystem health.^{1–5} The electrocatalytic nitrate reduction reaction (NO_3RR) is a promising approach to remediate nitrate by converting nitrate to products such as N_2 or NH_3 with a corresponding oxidation reaction such as oxygen or chlorine evolution.^{3,6–14} However, NO_3RR rates are hindered by the chloride present in many nitrate-laden waste streams. Streams containing both nitrate and chloride can arise from industrial effluent^{15–17} and the brine that comes from using ion exchange to separate nitrate contaminated water into clean water and concentrated nitrate.^{18,19} In addition to chloride inhibiting the rates, $\text{Cl}_2/\text{Cl}_3^-$ produced at the anode can cross over and corrode the NO_3RR electrocatalyst,^{20,21} which is particularly an issue for metal nanoparticle catalysts that are typically used to obtain high active surface areas.²² Understanding the effect of chloride

on NO₃RR and developing chloride-resistant nitrate reduction catalysts are both needed to create an effective electrocatalytic process that can remediate waste streams containing both nitrate and chloride. In this work, we demonstrate that rhodium sulfide on carbon (Rh_xS_y/C) is more active for NO₃RR than Pt/C and Rh/C in both the presence and absence of chloride. We also explain the rate-determining step (RDS) of NO₃RR on Pt, Rh, and Rh_xS_y and the chloride poisoning mechanism.

Catalytic inhibition of NO₃RR by chloride has been reported for Pt, Rh, Fe, and Cu electrodes,^{23–26} for which the reduction current is hypothesized to be suppressed by strong chloride adsorption on metals.^{26–29} NO₃RR occurs at potentials where both nitrate and hydrogen can adsorb (**Scheme 1**); for Pt and Rh this potential is between 0–0.3 V vs. RHE.^{3,30} Nitrate coverages are related to the free energy of nitrate adsorption (ΔG_{NO_3}) on a catalyst surface. Nitrate adsorption is favorable at potentials more positive than $\Delta G_{\text{NO}_3}/F$ ($E = 0$ V vs. SHE)/ F , where F is Faraday's constant. Hydrogen adsorption is favorable at potentials more negative than $\Delta G_{\text{H}}/F$, where ΔG_{H} is the hydrogen adsorption free energy at 0 V vs. RHE. Therefore, hydrogen covers the catalyst surface at negative potentials (**Scheme 1a**). Chloride adsorption is also potential-dependent, and chloride will adsorb at potentials more positive than $\Delta G_{\text{Cl}}/F$ ($E = 0$ V vs. SHE)/ F , where ΔG_{Cl} is the free energy of chloride adsorption. The potentials at which chloride adsorbs at high coverages may overlap with the potentials required for high NO₃RR activity.³¹ At these potentials (**Scheme 1b–c**), adsorbed chloride may block active sites for hydrogen and nitrate adsorption. We hypothesize that NO₃RR requires high coverages of both nitrate and hydrogen, so a decrease in hydrogen and nitrate coverage from competitive adsorption of chloride will decrease the reaction rate. Therefore, an ideal chloride-resistant catalyst should adsorb nitrate and hydrogen more strongly than chloride.



Scheme 1. Potentials and free energies associated with different adsorption and reaction events on electrode surfaces, including hydrogen evolution reaction (HER, gray potential window), nitrate adsorption (ΔG_{NO_3} , $\text{NO}_3^- + * \rightleftharpoons \text{NO}_3^* + e^-$), nitrate reduction reaction (NO₃RR, blue potential window), Cl⁻ adsorption (ΔG_{Cl} , $\text{Cl}^- + * \rightleftharpoons \text{Cl}^* + e^-$, green-hatched potential window), and hydrogen adsorption (ΔG_{H} , $\text{H}^+ + * + e^- \rightleftharpoons \text{H}^*$). The potential region where chloride, nitrate, and hydrogen are all present on the surface is the overlap of blue with green hatches. Representative electrode surface coverages are shown for a) HER, b) NO₃RR with Cl^{*}, and c) adsorbed chloride regions. F is Faraday's constant, used to convert between potentials and free energies. ΔG_{NO_3} , ΔG_{Cl} , and ΔG_{H} labeled on the scheme

are all the values at 0 V vs. SHE and pH = 0. Atom color legend: metal = gray; oxygen = red; nitrogen = blue; chlorine = green; hydrogen = white.

Herein, we study the performance of rhodium sulfide supported on carbon ($\text{Rh}_x\text{S}_y/\text{C}$) for NO_3RR as a potential chloride-resistant electrocatalyst and compare it to Pt/C and Rh/C to understand chloride poisoning and the NO_3RR mechanism. We choose Pt and Rh for study for several reasons: 1) they are two of the few metals that have previously been investigated and reported to be poisoned by chloride,^{23,24} motivating this study into the cause; 2) Pt binds nitrate weakly and Rh binds nitrate strongly,³⁰ allowing a comparison between two different systems to investigate whether chloride poisoning is different; and 3) Pt and Rh are both active for nitrate reduction in the potential range where hydrogen evolution is not thermodynamically possible (>0 V vs. RHE), making it experimentally simpler to study nitrate reduction, as the reduction current comes solely from nitrate reduction, rather than a mixture of hydrogen evolution and nitrate reduction. We study Rh_xS_y because Rh is the most active platinum group metal for NO_3RR and Rh_xS_y is known to be halide-resistant for electrocatalytic oxygen reduction and hydrogen evolution.^{22,32–39} Our experiments show that $\text{Rh}_x\text{S}_y/\text{C}$ is more active for NO_3RR than Rh/C when the activity is normalized to the number of surface sites. In the presence of 1 mM Cl^- , however, $\text{Rh}_x\text{S}_y/\text{C}$ has only slightly better poison resistance than Rh/C and Pt/C (i.e., with 1 mM Cl^- the NO_3RR current decreases 33–42% for $\text{Rh}_x\text{S}_y/\text{C}$, 32–52% for Pt/C, and 56–63% for Rh/C between 0.05–0.2 V vs. RHE at pH 0 with 1 M NaNO_3). To rationalize the NO_3RR rate inhibition observed between $\text{Rh}_x\text{S}_y/\text{C}$, Pt/C, and Rh/C, we develop a microkinetic model based on our experimental results and perform density functional theory (DFT) calculations. Our experimental rate measurements on Pt/C are qualitatively explained by a rate law for NO_3RR where the RDS is the surface reaction between adsorbed H and adsorbed nitrate. Our rate measurements on Rh/C match the rate laws where the RDS is a surface reaction between adsorbed H and adsorbed nitrate or direct deoxygenation of nitrate to nitrite without the addition of H. Our DFT calculations do not find a feasible pathway on Rh for adsorbed H and adsorbed nitrate to react, whereas the direct deoxygenation of nitrate to nitrite without the addition of H is found. DFT-predicted linear scaling relations between the adsorption free energies of nitrate and chloride on transition metals show that a metal that adsorbs nitrate strongly will also adsorb chloride strongly. The competition for surface sites between chloride and nitrate, combined with their linear adsorbate scaling relations explains why Pt and Rh are poisoned similarly by chloride for NO_3RR , despite Rh binding nitrate more strongly. DFT calculations predict that pristine Rh_xS_y terraces adsorb nitrate too weakly to yield high NO_3RR activity. However, Rh_xS_y terraces with sulfur (S) vacancies adsorb nitrate strongly, and the S-defected Rh_3S_4 surface has a low enough activation barrier for direct nitrate dissociation to be responsible for the observed NO_3RR activity. Additionally, this S-defected Rh_3S_4 surface binds chloride strongly and follows adsorbate linear scaling similar to the transition metal surfaces, thus explaining the weaker-than-expected chloride resistance for $\text{Rh}_x\text{S}_y/\text{C}$ toward NO_3RR . The combined experimental and computational findings reported here clarify the role of chloride poisoning of NO_3RR catalysts and the importance of considering S vacancies for metal sulfide electrocatalysts.

2. EXPERIMENTAL AND COMPUTATIONAL METHODS

2.1. Electrocatalyst preparation.

A Pt rotating disk (Pine Research Inst., Inc.), a Rh wire (99.8%, Alfa Aesar), 30 wt% Pt/C (Fuel Cell Store), 20 wt% Rh/C (Fuel Cell Store), and 30 wt% Rh_xS_y/C (details of catalyst available in refs.^{22,34,40}) were used as catalysts. The Pt rotating disk electrode (RDE) was hand-polished using a 0.05 μm alumina suspension (Allied High Tech Products, Inc.) on a micropolishing cloth and ultrasonicated in deionized water (18.2 MΩ cm, Millipore Milli-Q system) for 30 minutes before assembling in the Teflon rotating disk holder. Subsequently, the assembled Pt RDE was electrochemically cleaned in the supporting electrolyte from –0.2 to 1.2 V vs. RHE at 100 mV s⁻¹ for 50 cycles. The Rh wire was flame-annealed, then electrochemically cleaned in the supporting electrolyte from –0.2 V to 1.0 V vs. RHE at 100 mV s⁻¹ for 50 cycles.

All catalysts supported on carbon were deposited in the form of a prepared ink on a glassy carbon disk. The catalyst inks were prepared by combining 3 mg of supported catalyst (Rh_xS_y/C, Rh/C, or Pt/C) with 5 mL of 50:50 deionized water and isopropanol mixture in a scintillation vial. 17.5 μL of 5 wt% Nafion solution (5 wt% Nafion, Sigma Aldrich) in isopropanol was added and the vial was ultrasonicated for two hours. 8 μL catalyst ink was deposited twice on a clean glassy carbon disk (Pine Research Inst., Inc), allowing the disk to air-dry between depositions. Prior to measurements, the catalysts deposited on glassy carbon were electrochemically cleaned (–0.2 to 1.2 V vs. RHE at 100 mV s⁻¹ for 50 cycles for Pt/C, –0.2 to 0.75 V vs. RHE at 50 mV s⁻¹ for 50 cycles for Rh/C, and –0.2 to 0.75 V vs. RHE at 50 mV s⁻¹ for 50 cycles for Rh_xS_y/C).

2.2. Electrochemically active surface area and hydrogen underpotential deposition.

Hydrogen underpotential deposition (H_{upd}) was used to determine the electrochemically active surface area (ECSA) for Pt and Rh (RDE, wire, and supported catalysts). The Pt and Rh electrodes were cycled at 100 mV s⁻¹ from 0.05 to 1.2 V vs. RHE and 0.05 to 1.0 V vs. RHE, respectively. A three-electrode electrochemical setup was used with a Pt wire (99.99%, Pine Research Inst., Inc.) counter electrode and a double junction Ag/AgCl (10% KNO₃ outer solution/4 M KCl inner solution, Pine Research Inst., Inc.) reference electrode. A two-compartment cell was used in which the compartment with the working electrode and reference electrode was separated from the counter electrode compartment using a Nafion 117 membrane. The supporting electrolyte was 1 M H₂SO₄ prepared from concentrated H₂SO₄ (99.999%, Sigma Aldrich) for Rh and 1 M HClO₄ prepared from 61% HClO₄ (Fisher Chemical) for Pt. For Rh, H₂SO₄ was selected instead of HClO₄ because perchlorate poisons the Rh surface via reduction to chloride^{41,42} whereas bisulfate and sulfate anions are not known to interact strongly with Rh. HClO₄ was selected as the supporting electrolyte for Pt measurements because the perchlorate anion adsorbs less strongly than bisulfate and sulfate anions on Pt, which interfere with H_{upd}.^{23,43} Electrolytes were sparged with N₂ (99.999%, Cryogenic Gases) for 60 min before use. All electrochemical measurements were collected using a VSP potentiostat (Bio-Logic Science Inst.). For Pt and Rh, a baseline double-layer charging current was measured at 0.4 V vs. RHE and subtracted to determine only the H_{upd} charge from the hydrogen desorption process (**Figure S1**). This H_{upd} desorption charge was used to calculate the ECSAs for Pt and Rh using average charge densities of 210 and 221 μC cm⁻², respectively.⁴⁴

For Rh_xS_y/C, the ECSA was approximated by first using cyclic voltammetry in the non-faradaic region (0.45 to 0.75 V vs. RHE) as a function of the scan rate (100 to 20 mV s⁻¹) to determine the total capacitance associated with the electrochemical double layer (for both carbon and Rh_xS_y). The total capacitance, Rh_xS_y particle sizes, weight loading, specific capacitance, and specific area of carbon were used to approximate

the ECSA of Rh_xS_y (approximating the Rh_xS_y particles as cubes; see ESI).^{45,46} All particle sizes were determined using X-ray powder diffraction (XRD, **Figure S2**) and crystallite sizes were estimated using the Scherrer equation. Particle size distributions were measured using transmission electron microscopy (**Figure S3**), with the mean particle size of $\text{Rh}_x\text{S}_y/\text{C}$ slightly lower than that observed by XRD. Effects of the differences between XRD and TEM particle sizes and size distribution on the ECSA estimates are discussed in the ESI. This capacitance & XRD method estimates ECSA within 53% of H_{upd} values compared to Pt/C and Rh/C (**Table S1**), giving confidence in the ability for it to accurately estimate ECSA for $\text{Rh}_x\text{S}_y/\text{C}$. The Rh_xS_y crystallites used were 12 nm in diameter. For Pt/C and Rh/C, the crystallite sizes were 2.2 nm and 2.3 nm, respectively. The Rh_xS_y surfaces are not metallic Rh under reaction conditions based on a lack of observable H_{upd} charge (**Figure S1**) and the absence of metallic Rh using XRD (**Figure S2**).

2.3. Steady-state electrocatalytic nitrate reduction reaction measurements.

The same three-electrode, two-compartment electrochemical cell setup used to determine the ECSA was used for steady-state current measurements. The working electrolyte was purged with N_2 for 60 minutes prior to measurements. NO_3RR activity was measured under steady-state conditions by performing constant potential electrolysis for 2 hours, where the reported current is the steady-state current that was reached. Steady-state measurements were taken at room temperature (23 °C). All measurements were taken at a RDE rotation rate of 2500 rpm to minimize the concentration gradient between the electrode surface and the bulk solution. The effect of rotation rate and a comparison of the results in 1 M HNO_3 to those with 1 M NaNO_3 are discussed in **Figure S4**. Loss of catalyst due to poor adhesion to the glassy carbon disk was less than 11% of the ECSA, based on the capacitance before and after steady-state measurements. Electrochemical impedance spectroscopy was used to measure the series resistance, but because the currents were low, the ohmic resistance corrections to the voltage were less than 1 mV. The steady-state current with and without chloride for each potential was taken via individual experiments. The concentration of chloride was chosen as 1 mM to probe the effect of poisoning, which is in the lower range of chloride concentrations in wastewater and ion exchange brine streams (0.14 mM to 2.8 M Cl^-).^{15–19,47} We also explored 10 and 100 mM Cl^- to test how higher chloride concentration affected poisoning. For supported $\text{Rh}_x\text{S}_y/\text{C}$, Pt/C, and Rh/C, the measurements were repeated three times, but each time a new catalyst was used to prevent any loss of material because of adhesion issues. Pt/C and Rh/C currents were normalized to the ECSA obtained by H_{upd} and $\text{Rh}_x\text{S}_y/\text{C}$ currents were normalized to the approximated ECSA from the capacitance & XRD method. Each current measurement was normalized to the ECSA to account for differences in catalyst weight loading (30 wt% Pt/C, 20 wt% Rh/C, and 30 wt% $\text{Rh}_x\text{S}_y/\text{C}$) and variation in individual ink depositions. This method of normalizing resulted in the same current densities reported even for different amounts of a given catalyst deposited onto the electrode.

2.4. Product quantification.

For measurements of the faradaic efficiency, the commercial $\text{Rh}_x\text{S}_y/\text{C}$ and Rh/C powders were loaded onto carbon felts (6.35 mm thick, 99.0%, Alfa Aesar) instead of the glassy carbon disk to increase the amount of catalyst loading to enable sufficient product formation detectable in a reasonable amount of time. The carbon felts were pretreated thermally at 400 °C with H_2 at 60 psi for four hours. A catalyst ink was prepared by combining 10 mg of supported catalyst ($\text{Rh}_x\text{S}_y/\text{C}$ or Rh/C) with 1.5 mL isopropanol and 1 mL deionized water in a scintillation vial and sonicating for 10 minutes. The catalyst ink was deposited onto the thermally treated carbon felt (1 cm × 3 cm) and allowed to dry. The carbon felt with catalyst was then attached to a

graphite rod (6.15 mm diameter, 99.9995%, Alfa Aesar). Prior to nitrate conversion, the catalyst on carbon felt was electrochemically cleaned in 1 M H₂SO₄ (N₂-sparged) by cycling the potential as described above. The electrochemical cleaning was completed in a single-compartment electrochemical cell with a graphite rod counter electrode and double-junction Ag/AgCl reference electrode. After cleaning, the catalyst on carbon felt was then transferred to a two-compartment electrochemical cell for the product quantification measurements (with the same electrochemical set up used for steady-state current measurements). The working electrolyte was 0.1 M HNO₃ (N₂-sparged). Because of the higher currents enabled by the larger catalyst surface area, 85% of the voltage drop due to solution resistance was compensated for during the measurement. The remaining 15% amounted to less than 15 mV on average. For measuring the faradaic efficiency, 0.1 V vs. RHE was chosen because this was the potential with the highest nitrate reduction current without background currents observed from the supporting electrolyte (**Figure S22**). The faradaic efficiency for Pt/C at these conditions (0.1 V vs. RHE, 0.1 M HNO₃) has been reported as almost 100% towards ammonium.¹⁰

The products formed were determined by extracting 0.5 mL aliquots of the solution in the electrochemical cell every hour during operation and storing them at room temperature until all measurements were taken. A portion of each aliquot was used for NO₃⁻, NO₂⁻, and NH₄⁺ quantification separately. NO₃⁻ and NO₂⁻ were detected using standard spectrophotometric methods⁴⁸ and NH₄⁺ was detected using the indophenol blue test^{49,50} (described in the ESI). After appropriate dilution, the sample was transferred into a quartz cuvette with a 1 cm pathlength, and the UV-Vis spectra was taken using a UV-Vis spectrophotometer (Evolution 350, Thermo Scientific). Concentrations were determined using the absorbances against prepared standard calibration curves (**Figure S5**).

2.5. Cyclic voltammetry studies of chloride adsorption.

Adsorption of chloride and hydrogen on the Pt rotating disk and Rh wire was studied via the H_{upd} charge in HClO₄ and H₂SO₄ with NaCl (≥ 99.5%, Sigma Aldrich) concentrations of 0, 0.001, 0.01, 0.1, and 0.15 M Cl⁻. The setup and operation were the same as for H_{upd} to measure the ECSA, other than the addition of chloride. The chloride concentration was adjusted by adding small volumes (less than 0.5 mL) of concentrated chloride solution to the electrochemical cell at room temperature. After addition, the solution was stirred and sparged with N₂ for 10 minutes. Polycrystalline surfaces (RDE and wire) were used for cyclic voltammograms because they have more well-defined H_{upd} peaks than the carbon-supported nanoparticle catalysts.

2.6. Atomistic modeling details.

2.6.1. Geometry relaxation and transition state search

DFT calculations were performed using the Vienna Ab Initio Simulation Package⁵¹⁻⁵⁴ with the BEEF-vdW functional.⁵⁵ BEEF-vdW exhibits similar or superior performance compared to functionals such as PBE, RPBE, and optPBE-vdW.⁵⁶ BEEF-vdW includes a van der Waals correction and yields its own error estimates of electronic energies. All calculations were spin-polarized and used the projector-augmented wave method,^{57,58} a plane-wave kinetic energy cutoff of 400 eV, and Gaussian smearing of 0.05 eV. Geometry optimizations used differences of less than 0.02 eV Å⁻¹ for ionic steps and 10⁻⁴ eV for electronic steps as stopping criteria. Geometry optimization was done for bulk crystals to calculate lattice constants using a Γ -centered Monkhorst-Pack k -point grid (16×16×16 for metals, 4×4×4 for Rh_xS_y structures).⁵⁹ For metal surfaces, a 6×6×1 k -point grid was used, and slabs were built using a 3×4×4 supercell of the (211) facet. The bottom layer of atoms was fixed, and all other layers could relax, with 13 Å of vacuum space.

The adsorption energies of NO_3^- , Cl^- , and H^+ were computed for the (211) stepped surfaces of Au, Ag, Cu, Pd, Pt, and Rh. Adsorption energies were calculated using coverages of 1/12 ML (for H^+ and Cl^-) or 1/6 ML (for NO_3^-). We choose (211) as a model site that is reported to be active for NO_3RR .^{30,60,61} The choice of the (211) is also validated by our previous computational work, which reproduced experimental NO_3RR activity trends on transition metals using a microkinetic model built on step surface data.³⁰ For the (211) facet used, we extensively sampled possible adsorption sites on both the edge and terrace portions of this facet (see **Figure S11** in the ESI). The adsorption site selected was that with the most negative binding energy, which was the edge site on the (211) facet.

For models of pristine and S-defected Rh_xS_y surfaces (i.e., with sulfur vacancies), adsorption energies were calculated using a $3\times 3\times 1$ k -point grid, with other DFT settings kept the same as used for metal surfaces. To simulate similarly low coverages of adsorbates, each Rh_xS_y slab was repeated in the x and/or y directions to create a larger supercell such that the entire slab contained no more than 80 slab atoms. Enough layers were maintained in each supercell such that the slab thickness was approximately 8–10 Å. During geometry optimization, the bottom half of each Rh_xS_y slab was constrained and all other atoms could relax, with 38 Å of vacuum space. Electronic energies of isolated H_2 , N_2 , Cl_2 , HCl , HNO_2 , HNO_3 , NO_3 , and NO_2 species in the gas phase were calculated using the same DFT settings as used for pure metals, but with a plane-wave energy cutoff of 500 eV, Gaussian smearing of 0.2 eV, and a $1\times 1\times 1$ k -point grid. To minimize interference of periodic images and excess symmetry, each gas-phase adsorbate was placed slightly off-center in a $15.00\times 15.11\times 15.21$ Å cell.

Nitrate adsorption free energies in the aqueous phase were calculated at standard conditions (298.15 K, 1 M) via a thermodynamic cycle. Aqueous-phase solvation effects on surface energies, chloride and hydrogen adsorption, and transition state energies were not included. See ESI and accompanying discussion for more detail on the thermodynamic cycle (**Figure S6** and **Tables S2 and S3**) and DFT benchmarking tests (**Figures S7 and S8**).

Nitrate dissociation activation energies on Rh and Rh_xS_y phases were identified using the climbing-image nudged elastic band method (NEB) method⁶² (for the direct reduction mechanism) or the improved dimer method^{63,64} (for the H-assisted reduction mechanism). Activation energy calculations on Rh and Rh_xS_y surfaces used the same DFT settings as used for geometry relaxations on pure metal and Rh_xS_y surfaces, with spring forces of 5 eV \AA^{-1} and with a climbing image used throughout the relaxation. All endpoints and transition states for the transition state calculations are shown in **Figures S14–S17**. The dimer method used a dimer length of 0.01 Å and step sizes ranging from 0.0018 Å to 0.0075 Å. The initial dimer images were estimated using an interpolated image slightly earlier than the transition state image predicted by NEB and atomic displacements tangent to the NEB curve at the transition state reaction coordinate, respectively. Initial trial dimer directions were estimated by inspection, by randomly displacing atoms in the adsorbate, and by calculating eigenvectors from vibrational analysis of the initial dimer images. As with NEB and geometry relaxations, dimer optimization used an electronic tolerance of 10^{-4} eV and a maximum ionic force tolerance of 0.02 eV \AA^{-1} .

2.6.2. Surface facet and termination choice for model Rh_xS_y systems

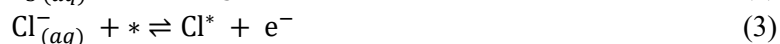
Rh_xS_y is a mixture of Rh_3S_4 , Rh_2S_3 and $\text{Rh}_{17}\text{S}_{15}$ phases. The bulk phase stability of Rh_xS_y has been determined using electrochemical measurements,⁶⁵ which concluded that Rh_2S_3 is the enthalpically most stable bulk phase by about 2 kJ mol^{-1} , followed by Rh_3S_4 and then $\text{Rh}_{17}\text{S}_{15}$, although experiments and theory disagree about this ordering.⁶⁶ Prior DFT modeling predicted stable surface terminations of low-index Rh_xS_y facets (i.e., $\text{Rh}_2\text{S}_3(001)$, $\text{Rh}_3\text{S}_4(100)$, and $\text{Rh}_{17}\text{S}_{15}(100)$) in the gas phase.³⁴ Based on this study, we chose to

model adsorption and reactions on the termination of the lowest surface energy for each of these facets in the gas phase. For Rh_xS_y there are many possible locations along the facet's normal vector to cut the surface that will lead to different surface terminations (**Figure S9**). The Pymatgen software package^{67,68} was used to search for symmetrically distinct surface terminations of these facets in a more exhaustive way than the prior study.³⁴ Symmetric terminations were enumerated from the $\text{Rh}_2\text{S}_3(001)$, $\text{Rh}_3\text{S}_4(100)$, and $\text{Rh}_{17}\text{S}_{15}(100)$ facets using a per-atom surface energy metric (additional details provided in the ESI). With a tolerance of 0.1 Å between successive cleave planes, 26 symmetrically unique terminations (five for $\text{Rh}_2\text{S}_3(100)$, nine for $\text{Rh}_3\text{S}_4(100)$, and 12 for $\text{Rh}_{17}\text{S}_{15}(100)$) were found. The most stable surface terminations are reported in **Figure S10**. Ultimately, our identified low-energy surface terminations agree with the previous study of Rh_xS_y .³⁴ We emphasize these are vacuum-phase model systems and that there may be surface reconstruction under acidic conditions and in the presence of an applied potential.⁶⁹ Nevertheless, we show that these model surfaces qualitatively rationalize our experimental observations.

To model Rh_xS_y surfaces with S vacancies, a single S atom was removed from each of the three pristine surface terminations that we identified as most stable. For each of these pristine surface terminations, the symmetrically distinct surface S atoms were located. A single S atom was removed at a time and the resulting energy of the defected surface calculated. The position of the S vacancy resulting in the lowest surface electronic energy was chosen as the vacancy position for that termination and was used when modeling adsorption of species (**Figure S13**). To limit complexity and computational expense, we limited our study to vacancies of only a single S atom in the supercell.

2.7. Langmuir adsorption model and Langmuir-Hinshelwood reaction model.

For an aqueous system with nitrate and chloride present, NO_3^- , Cl^- , and H^+ can occupy active catalyst sites (denoted as *). The equilibrium coverage of hydrogen, nitrate, and chloride is modeled assuming Langmuir competitive adsorption between the species (**Eq. 1–3**).



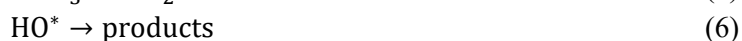
We assume that one electron is transferred per adsorbed chloride,²⁷ hydrogen, and nitrate based on previous measurements (**Figure S18**)³⁰ and our work shown below. Because of this electron transfer, the coverage of each species is a function of the electrode potential.

Nitrate dissociation is typically considered the RDS for NO_3RR , as experimentally observed for Pt and Rh under acidic conditions^{43,70} and predicted for metals.³⁰ Direct nitrate reduction to selected products was modelled in our previous work, based on a microkinetic model of 19 elementary reactions.³⁰ Degree of rate control analysis showed that nitrate dissociation to nitrite and oxygen was rate controlling on Pt and Rh, which was modeled with **Eq. 4** as the RDS. Assuming the adsorption steps (**Eqs. 1–3**) are quasi-equilibrated and the further reactions of adsorbed nitrite and oxygen (**Eqs. 5–7**) are infinitely fast, the rate law for direct nitrate dissociation as the RDS is **Eq. 8**.



$$\text{rate} = \frac{k_4 K_{\text{NO}_3} [\text{NO}_3^-]_0}{(1 + K_{\text{H}} [\text{H}^+]_0 + K_{\text{NO}_3} [\text{NO}_3^-]_0 + K_{\text{Cl}} [\text{Cl}^-]_0)^2} \quad (8)$$

K_{H} , K_{NO_3} , and K_{Cl} are the potential-dependent equilibrium adsorption constants of **Eqs. 1–3** and $[\text{NO}_3^-]_0$, $[\text{H}^+]_0$, and $[\text{Cl}^-]_0$ are the bulk concentration of each species in the solution. The rate constant k_4 is the rate constant for the forward reaction in **Eq. 4**. However, the rate law in **Eq. 8** that assumes direct nitrate dissociation is the RDS disagrees with experimental results shown in this work for Pt/C. Instead, a microkinetic model using the H-assisted nitrate dissociation to nitrite via a surface reaction of adsorbed nitrate and adsorbed hydrogen (**Eq. 9**) as the RDS resulted in a rate law that more closely matches our experimental observations for Pt/C.



Previous work has proposed an H-assisted nitrate dissociation mechanism via adsorbed HNO_3 on metal and oxide surfaces.^{71,72} For subsequent analysis, we assume the H-assisted nitrate dissociation shown in **Eq. 9** is the RDS and thus approximate the adsorption steps (**Eqs. 1–3**) of nitrate, chloride, and protons to be quasi-equilibrated. We assume that the formed hydroxide and nitrite on the surface (**Eqs. 6 and 7**) instantaneously react to form other products or leave the surface. Although the reaction in **Eq. 9** may not correspond to an actual elementary step (if HNO_3 is a stable surface intermediate), we assume that it follows an elementary rate law in this work. Thus, the rate equation for NO_3RR is:

$$\text{rate} = k_9 \theta_{\text{NO}_3} \theta_{\text{H}} \quad (10)$$

where θ_i is the surface coverage of species i , k_9 is the reaction rate constant for the forward reaction in **Eq. 9**, and the site balance is $1 = \theta_{\text{H}} + \theta_{\text{NO}_3} + \theta_{\text{Cl}} + \theta_*$. The coverages of the different species can be determined by assuming that the reactions in **Eqs. 1–3** are quasi-equilibrated. This would result in a rate law shown in **Eq. 11**. Although the full microkinetic model is more complex, we show that this Langmuir-Hinshelwood model qualitatively predicts the observed inhibition of nitrate reduction in the presence of chloride.

$$\text{rate} = \frac{k_9 K_{\text{NO}_3} [\text{NO}_3^-]_0 K_{\text{H}} [\text{H}^+]_0}{(1 + K_{\text{H}} [\text{H}^+]_0 + K_{\text{NO}_3} [\text{NO}_3^-]_0 + K_{\text{Cl}} [\text{Cl}^-]_0)^2} \quad (11)$$

Two additional microkinetic models were explored, one using direct nitrate reduction by protons as the RDS and the other considering nitrate dissociation and hydroxide formation with a pseudo-steady state hypothesis for the coverage of oxygen (**Figures S19–S21**). Their corresponding rate laws did not qualitatively match the experimental kinetic measurements and the rate law in **Eq. 11**, so they are not used for analysis.

3. RESULTS AND DISCUSSION

To better understand the NO_3RR activity and mechanism on Pt, Rh, and Rh_xS_y in the presence of chloride, in the following sections we: (i) compare Rh_xS_y activity for nitrate reduction against that of Pt and Rh, (ii) examine the competition between chloride and nitrate adsorption on Pt and Rh, (iii) provide a kinetic model

that rationalizes chloride poisoning of NO₃RR on Pt and Rh, (iv) explain chloride-poisoning trends via adsorbate scaling relationships between chloride and nitrate adsorption energies, and (v) propose a plausible active site of Rh_xS_y based on experimental and computational observations.

3.1. Rh_xS_y performance for nitrate reduction compared to Pt and Rh.

The steady-state reduction current densities as a function of potential in **Figure 1a** show Rh_xS_y/C has higher NO₃RR activity than Rh/C and Pt/C with and without chloride. Pt/C has much lower activity than either Rh_xS_y/C or Rh/C, attributed to its weaker nitrate adsorption.⁴³ Without nitrate, no current is detected for Rh_xS_y/C other than the onset of hydrogen evolution at 0 V vs. RHE (**Figure S22**). The reported activities are normalized to the ECSA, however the difference in particle size of Pt/C and Rh/C (2.2 and 2.3 nm, respectively) compared to Rh_xS_y/C (12 nm) may lead to differences in nitrate reduction activity due to differences in the fraction of step sites at the surface. On metals, stepped sites are reported to be more active than terraces.^{73,74} Thus, smaller particles sizes (with a higher fraction of step sites sites) would be expected to be more active on a per-surface-area basis. Although the Rh_xS_y/C has higher area-normalized activity than Rh/C, the former has lower ammonia faradaic efficiency. The faradaic efficiency for Rh_xS_y/C in 0.1 M HNO₃ is 67% to NH₄⁺ at 0.1 V vs. RHE (**Figure S23**). The NO₃RR products of Rh/C under the same conditions are mainly NH₄⁺ (92% faradaic efficiency). In 0.1 M NaNO₃ + 0.5 M H₂SO₄, nitrate reduction products on Rh have been posed to be either NO₂⁻ or NH₄⁺,⁴³ of which we confirm the formation of NH₄⁺ on Rh in this study. Rh has also been reported to have high selectivity towards NH₃/NH₄⁺ between pH of 3.7–7.2 and moderate NH₄⁺ production in more basic conditions (pH of 13 or 14).^{75,76} Nitrite was not detected under these conditions for either catalyst. The remaining 33% of the faradaic efficiency for Rh_xS_y/C could be due to the formation of species such as NH₂OH, N₂, N₂O, or NO.

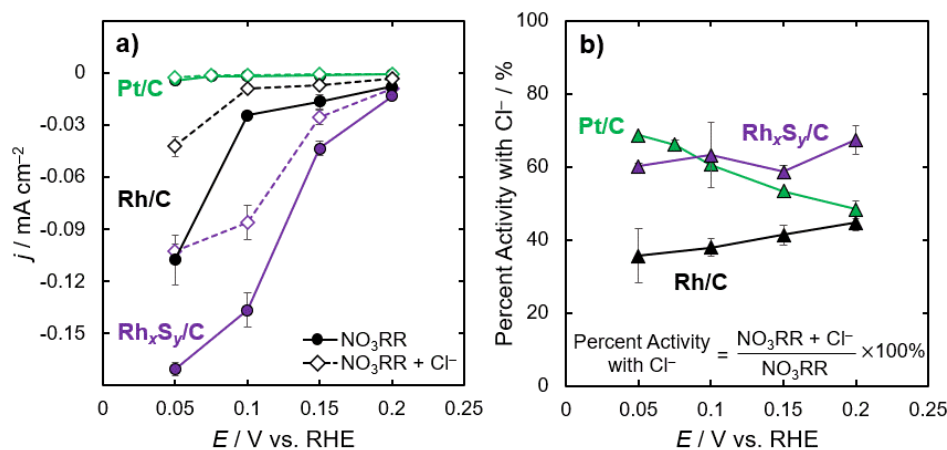


Figure 1. a) Steady-state nitrate reduction current density (j) on Pt/C (1 M HClO₄ + 1 M NaNO₃) and Rh/C and Rh_xS_y/C (1 M H₂SO₄ + 1 M NaNO₃) deposited on a glassy carbon rotating disk electrode at 2500 rpm rotation rate both without (filled circles) and with 1 mM Cl⁻ (open diamonds). Pt/C and Rh/C were normalized to the H_{upd} determined ECSA, and Rh_xS_y/C was normalized to the capacitance & XRD estimated ECSA. b) The percent nitrate reduction current (filled triangles) from the reduction currents with and without 1 mM Cl⁻ is shown for Rh/C, Pt/C, and Rh_xS_y/C for the potentials 0.05–0.2 V.

The steady-state current density measurements for all catalysts in **Figure 1** show a decrease in NO₃RR activity in the presence of 1 mM Cl⁻. The lower reaction rates on Pt/C and Rh/C due to chloride poisoning are similar to previous reports (**Figure S24** and **Table S5**). The faradaic efficiency towards NH₄⁺ for Rh/C

is not significantly changed with the addition of 1 mM Cl^- (**Figure S23**). Thus, the decrease in conversion rate of nitrate was decreased proportionally to the decrease in current density when chloride is present. The NO_3RR activity in the presence of Cl^- relative to the NO_3RR activity in the absence of chloride for $\text{Rh}_x\text{S}_y/\text{C}$, Rh/C , and Pt/C is shown as a function of potential in **Figure 1b**; the decrease in activity is more severe on Rh/C than Pt/C or $\text{Rh}_x\text{S}_y/\text{C}$. The NO_3RR activity when chloride is present decreases for Pt/C with increasing potential but increases or stays constant with increasing potential for Rh/C and $\text{Rh}_x\text{S}_y/\text{C}$. Chloride concentrations above 1 mM cause more severe inhibition on both Pt/C and Rh/C (**Figure S25**). Increasing the chloride concentration would increase the chloride coverage so greater NO_3RR inhibition is expected.

3.2. Competitive adsorption of Cl^- with H^+ on Pt and Rh.

To explain the inhibition of NO_3RR on Pt and Rh when chloride is present, we probe the adsorption of chloride on these surfaces. The competitive adsorption of Cl^- with H^+ on polycrystalline Pt and Rh is studied using cyclic voltammetry as a function of chloride concentration (1 mM–0.1 M Cl^-) between 0.05–0.4 V vs. RHE (**Figure 2a–b**). Because Rh_xS_y does not show hydrogen underpotential deposition (H_{upd}), the same study cannot be done on it. Without chloride, the measured anodic currents are due to electron transfer associated with underpotentially deposited hydrogen (H^*) desorbing from the surface (**Eq. 1**). The total anodic charge in the absence of chloride, Q_0 , taken by integrating the current with respect to the time of the anodic sweep, is proportional to the change in surface coverage of adsorbed hydrogen when changing the potential from 0.05 to 0.4 V vs. RHE. For Pt and Rh without chloride, Q_0 corresponds to approximately one monolayer of adsorbed hydrogen. We denote the charge in the presence of chloride as Q and plot the ratio of Q to Q_0 for Rh and Pt in **Figure 2c**. One effect of chloride on Q is that chloride prevents hydrogen from adsorbing, so there is less than one monolayer of adsorbed hydrogen to desorb, decreasing the observed charge ($Q/Q_0 < 1$). **Figure 2a** reveals that on Rh the current decreases with increasing chloride concentration. The decrease in current is attributed to the presence of chloride on the surface at these potentials, in which the adsorbed chloride blocks available sites for hydrogen to adsorb, reducing the total anodic charge observed (**Figure 2c**). We hypothesize that chloride has adsorbed at potentials more negative than 0.05 V vs. RHE on Rh, and the chloride coverage from 0.05 to 0.4 V vs. RHE is constant. Thus, there is no additional charge from chloride adsorption at these potentials and on Rh the only anodic current observed in **Figure 2a** comes from the desorption of H^* , which is less in the presence of chloride.

The current from the anodic scan and charge for Pt with increasing chloride concentration are shown in **Figure 2b–c**, respectively. In the absence of chloride, the Pt current has characteristic H_{upd} peaks that correspond to step and terrace sites that adsorb hydrogen at different potentials instead of a single broad peak for all adsorption sites like on Rh.^{77,78} The surface sites corresponding to the different H_{upd} peaks have been identified using a combination of single crystal studies and DFT modeling studies.^{61,79–82} When the chloride concentration is increased, the H_{upd} peaks shift toward lower potentials, making it challenging to deconvolute the different surface sites. The behavior on Pt is different from that of Rh, most notably that on Pt the anodic charge increases with the addition of small concentrations of chloride ions ($Q/Q_0 > 1$), and the charge only decreases at the highest tested chloride concentrations (**Figure 2c**). This increase in anodic charge may seem counterintuitive, as it implies that the hydrogen coverage is higher in the presence of chloride. However, as the potential is increased on Pt chloride is also adsorbing on the surface,^{83,84} which contributes additional anodic charge due to the electron transfer from the negatively charged chloride ion. Thus, the chloride coverage is increasing on Pt from 0.05 to 0.4 V vs. RHE. The observation from the experimental cyclic voltammograms that chloride is adsorbed at more negative potentials on Rh (<0.05 V

vs. RHE as discussed above) than on Pt (0.05–0.4 V vs. RHE), indicates that Rh binds chloride more strongly than Pt based on the Nernst equation.

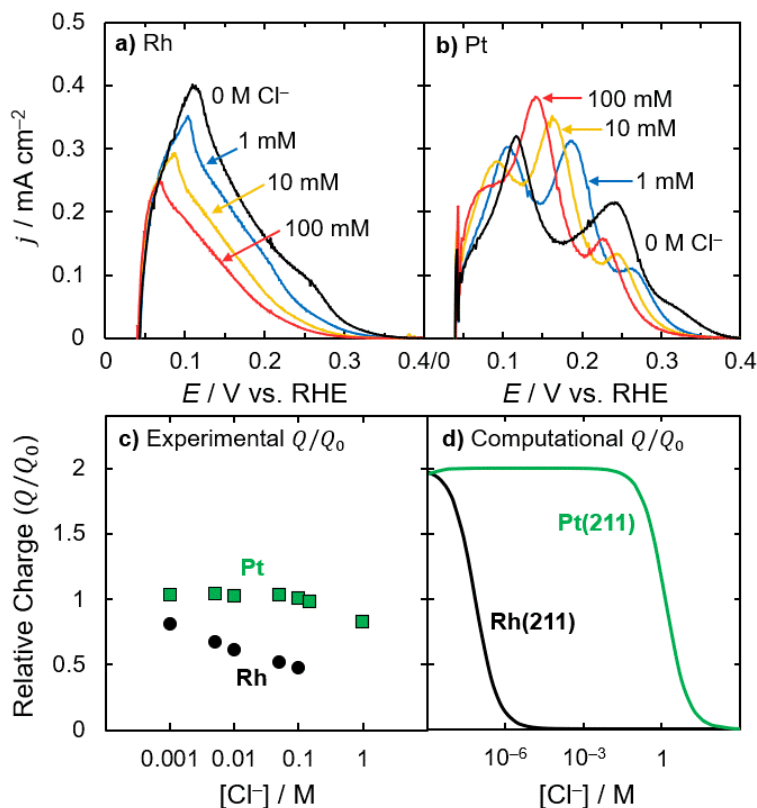


Figure 2. The anodic current during an oxidative scan as a function of potential for different concentrations of Cl⁻ on a) Rh wire in 1 M H₂SO₄ and b) Pt RDE in 1 M HClO₄ at 100 mV s⁻¹. c) Relative charge (Q/Q_0) of H_{upd} (0 to 0.4 V vs. RHE) on Rh wire and Pt RDE from a) and b), respectively. d) Computational Q/Q_0 on Rh(211) and Pt(211) were constructed by modeling the surface coverages of hydrogen and chloride from 0 to 0.4 V vs. RHE based on DFT modeling and assuming a scan rate of 100 mV s⁻¹. Rh and Pt are represented by black circles and green squares, respectively.

To better interpret the experimental cyclic voltammograms, we use DFT modeling to calculate the ΔG_{Cl} and ΔG_H on Rh and Pt and construct adsorption isotherms and computational cyclic voltammograms. The competitive Langmuir adsorption isotherm is used to predict equilibrium coverages as a function of applied potential. We model (211) stepped sites because they bind nitrate more strongly than terraces and are hypothesized to be active sites for NO₃RR.^{30,60,61} For Rh(211) and Pt(211) the ΔG_{Cl} at 0 V vs. SHE are -56.2 kJ mol⁻¹ and -20.2 kJ mol⁻¹, respectively, qualitatively matching the cyclic voltammogram observations that chloride binds more strongly to polycrystalline Rh than to Pt. The ΔG_H on Rh(211) and Pt(211) are -17.4 and -23.5 kJ mol⁻¹, respectively at 0 V vs. RHE. The coverages of chloride and hydrogen on Rh(211) and Pt(211) are predicted as a function of potential using a single site adsorption model (**Figure S19a–b**). We computationally predict cyclic voltammograms for Pt(211) and Rh(211) with and without chloride (**Figure S19c–d**), assuming for each potential the surface reaches equilibrium, and show the predicted charge in **Figure 2d**. We focus on qualitative trends between the two metals and with increasing chloride concentrations because the absolute values of the DFT-predicted adsorption energies are not quantitative because of challenges with predicting anion adsorption at solvated interfaces.⁸⁵

Additionally, as the experimental measurements are on polycrystalline Pt and Rh, the comparison between the experimental and computational results is qualitative.

The trends in charge from the computational cyclic voltammogram on Rh(211) and Pt(211) (**Figure 2d**) qualitatively agree with the experimental trends on Rh and Pt (**Figure 2c**). Chloride adsorbs strongly to the surface and competes with hydrogen to occupy sites. The decrease in the amount of adsorbed hydrogen is shown by the decrease in hydrogen adsorption charge on Rh(211) (**Figure 2d**). For Pt(211), the total charge is higher at low chloride concentrations and decreases at high chloride concentrations. From both the experimental and computational studies of hydrogen and chloride adsorption on Rh and Pt, we demonstrate that chloride interacts strongly with these metal surfaces by competitively occupying sites in the H_{upd} region, with chloride adsorbing more strongly on Rh than on Pt.

Based on the competitive Langmuir adsorption model, if we include nitrate adsorption then we expect that chloride and nitrate would compete to adsorb on the (211) sites. Due to this competition, the presence of chloride would cause a decrease in the nitrate coverage, and thus reduction rate. Because chloride adsorption is potential-dependent, this inhibition would also be potential-dependent.

3.3. Computational model of chloride poisoning of NO_3RR on Pt and Rh.

We expand the adsorption model assuming competitive adsorption among H^* , NO_3^* , and Cl^* and model the equilibrium coverages of these three species as a function of potential. The predicted equilibrium coverages are shown in **Figure 3a–b** for Rh(211) and Pt(211) at pH 0 with 1 M NO_3^- and 0 to 10^{-3} M Cl^- . For Rh(211) and Pt(211), the DFT-predicted ΔG_{NO_3} are $-1.44 \text{ kJ mol}^{-1}$ and 47.6 kJ mol^{-1} at 0 V vs. SHE respectively. The weaker adsorption of nitrate to Pt(211) than Rh(211) is consistent with previous reports.³⁰ For Rh(211), small concentrations of chloride greatly change the coverages of adsorbed species on the surface. Although Rh binds nitrate relatively strongly, chloride is bound even more strongly, and the equilibrium coverage is dominated by Cl^* . On Pt(211), nitrate has low coverage in this potential range, therefore the hydrogen coverage with and without 1 M NO_3^- is almost identical and the nitrate coverage approaches zero when chloride is present.

If we assume the RDS of NO_3RR is the surface reaction between nitrate and hydrogen (**Eq. 9**), the rate should be proportional to the coverage of nitrate times the coverage of hydrogen ($\theta_{\text{H}}\theta_{\text{NO}_3}$) as written in **Eq. 10**. The product of these two coverages on Rh(211) and Pt(211) is shown in **Figure 3c–d** both with and without chloride. The maximum in reaction rate for 0 M Cl^- is qualitatively similar to what has been observed experimentally for NO_3RR on these two surfaces.⁴³ Particularly, the maximum rate is at a more positive potential on Pt than on Rh due to the weaker adsorption of nitrate on Pt. As expected, chloride decreases $\theta_{\text{H}}\theta_{\text{NO}_3}$, supporting the hypothesis that the decrease in NO_3RR activity from chloride is from competitive adsorption of chloride. If we instead plot $\theta_*\theta_{\text{NO}_3}$, proportional to the rate law if the RDS is direct nitrate dissociation (**Eq. 4**) the same trend is seen for Rh(211) (**Figure S20a,c**), but the behavior on Pt(211) does not match our experimental data (**Figure S20e,g**), indicating Pt follows a H-assisted mechanism, whereas for Rh it is unclear which of the two mechanisms is occurring. Nitrate adsorbs stronger on Rh compared to Pt, nevertheless the Rh surface is poisoned more than that of Pt because of the stronger adsorption of chloride on Rh. This is evident by comparing the value of $\theta_{\text{H}}\theta_{\text{NO}_3}$ with and without chloride on Rh(211) and Pt(211) in **Figure 3c–d**, where the relative decrease is higher for Rh(211) at the same chloride concentration.

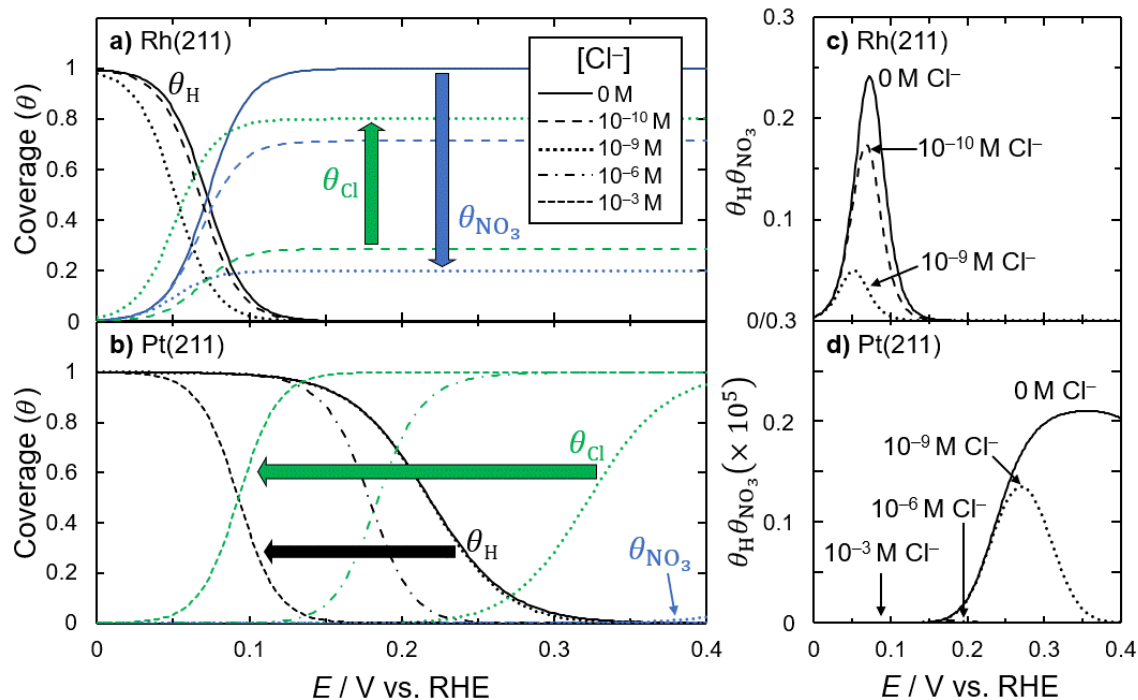


Figure 3. Predicted equilibrium coverage (θ) of hydrogen, chloride, and nitrate on a) Rh(211) and b) Pt(211) at pH 0 with nitrate (1 M NO₃⁻) and chloride (Rh: 10^{-10} M, 10^{-9} M; Pt: 10^{-9} M, 10^{-6} M, 10^{-3} M Cl⁻) assuming a single-site competitive adsorption model. Large arrows show direction of change in coverage as the chloride concentration is increased. The product of the equilibrium hydrogen and nitrate coverages is shown for c) Rh(211) and d) Pt(211) under the same conditions. Note that the data in d) is multiplied by 10^5 because of the low coverage of nitrate on Pt. Adsorbed species line color guide for a) and b): H* (black), NO₃* (blue), and Cl* (green).

The data in **Figure 3** shows that the decrease in $\theta_H \theta_{NO_3}$ in the presence of chloride is mainly from the decrease in the coverage of nitrate rather than a decrease in the hydrogen coverage. This effect is clearly demonstrated on Rh; as the concentration of chloride is increased from 0 M to 10^{-9} M Cl⁻, θ_H is only moderately decreased whereas θ_{NO_3} is considerably lowered (i.e., from 0 to 10^{-9} M Cl⁻ at 0.05 V vs. RHE, θ_H decreases from 0.8 to 0.5 and at 0.2 V vs. RHE, θ_{NO_3} decreases from almost full coverage to 0.2; see **Figure 3a**). A similar effect is observed with Pt at more positive potentials (where nitrate has a higher coverage). Therefore, although there is competition for sites between all three species, based on the adsorption energies the competition between the two adsorbing anions (Cl⁻ and NO₃⁻) is most responsible for the decrease in the NO₃RR rate. The reason that Rh is still poisoned by Cl⁻ even though Rh(211) binds NO₃⁻ more strongly than Pt(211) (by 49 kJ mol⁻¹) is that Rh(211) also binds Cl⁻ more strongly than Pt(211) by a similar amount (39 kJ mol⁻¹). By showing that the NO₃RR poisoning is due to the competition of nitrate and chloride we rationalize our experimental studies in **Figure 1** for Pt and Rh. At more positive potentials the chloride coverage is higher for Pt (**Figure 2c,d** and **Figure 3b**), explaining the higher inhibition in **Figure 1b** at more positive potentials. For Rh, where the coverage of chloride is more constant with potential (**Figure 2c,d**), the inhibition of the NO₃RR rate is more constant as shown in **Figure 1b**.

3.4. Modeling chloride and nitrate adsorption and nitrate dissociation on metals and rhodium sulfide.

Nitrate reduction is inhibited when chloride adsorbs strongly to the catalyst surface and blocks sites, thus we explore whether certain metals and Rh_xS_y can adsorb Cl^- weakly while adsorbing NO_3^- strongly. The Gibbs energies of adsorption for both NO_3^- and Cl^- on metal (211) surfaces are computed using the same methods as described for Rh(211) and Pt(211). The computed nitrate and chloride adsorption free energies are shown in **Figure 4a** at 0 V vs. SHE for the (211) surfaces of Ag, Au, Cu, Pd, Pt, and Rh. We observe a linear adsorbate scaling between the nitrate and chloride energies on these metals, indicated by the blue dotted line. The positive slope of the scaling relationship for metals implies that Cl^- adsorption energy increases concomitantly with the NO_3^- adsorption energy. Although Rh adsorbs NO_3^- more strongly than Pt, it also adsorbs Cl^- proportionally more strongly. Because of linear adsorbate scaling relationships and the fact that nitrate and chloride adsorption should shift similarly with potential, competitive adsorption of nitrate and chloride will be a persistent issue on many metals. This adsorbate scaling relation reveals that these metal surfaces would not be able to adsorb nitrate strongly (desired for NO_3RR activity) and adsorb chloride weakly (desired for resistance to chloride poisoning).

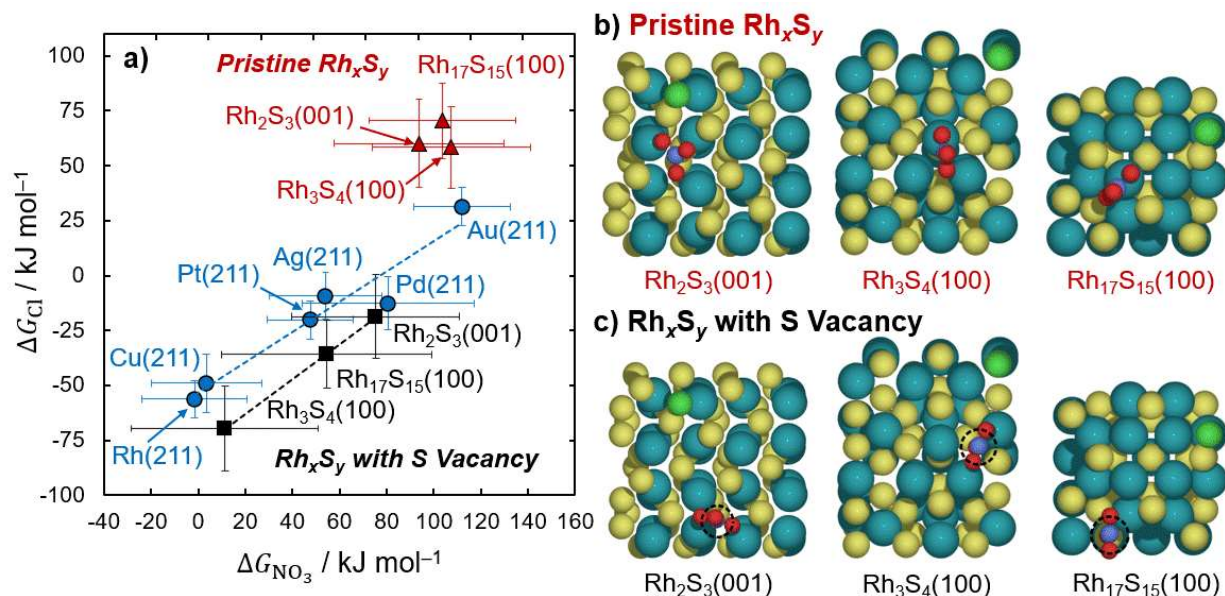


Figure 4. a) Computed Cl^- and NO_3^- adsorption Gibbs energies on metal (211) surfaces (blue circles), pristine Rh_xS_y surfaces (red triangles), and S-defected Rh_xS_y surfaces (black squares) at 0 V vs. SHE. The linear fit for metal (211) surfaces is $\Delta G_{Cl^-} = 0.69\Delta G_{NO_3^-} - 54 \text{ kJ mol}^{-1}$ with the coefficient of determination of the linear regression, $r^2 = 0.9338$. Linear fit for the Rh_xS_y surfaces with S vacancy is $\Delta G_{Cl^-} = 0.88\Delta G_{NO_3^-} - 75 \text{ kJ mol}^{-1}$ with $r^2 = 0.9997$. Error bars for uncertainties from the BEEF-vdW functional are shown. Top view of nitrate and chloride adsorption sites on b) pristine and c) S-defected Rh_xS_y surfaces. Teal = Rh, yellow = S, green = Cl, red = O, indigo = N, dashed circle = S vacancy.

Linear adsorbate scaling for one class of materials can be broken by moving to a different class of materials such as metal sulfides.⁸⁶ We predict that free energies of Cl^- and NO_3^- adsorption on the surfaces of pristine $Rh_2S_3(001)$, $Rh_3S_4(100)$, and $Rh_{17}S_{15}(100)$ are not constrained to the linear adsorbate scaling relationship established for metal (211) surfaces (**Figure 4a**). The Rh_xS_y surfaces shown in **Figure 4b** adsorb chloride more weakly relative to the metals. These Rh_xS_y surfaces (particularly Rh_3S_4) bind H^+ with

ΔG_{H} near 0 (ideal for hydrogen evolution/oxidation) while binding Cl^- weakly (**Figure S26**), which is why Rh_xS_y is more active for hydrogen evolution in the presence of halides (e.g., Cl^-) than metals.³⁸ However, for $\text{Rh}_x\text{S}_y/\text{C}$, we report a 33–42% inhibition of NO_3RR rate with 1 mM Cl^- (**Figure 1**), similar to the inhibition on Pt/C (32–52%) and Rh/C (56–63%), which indicates that the active site for NO_3RR on Rh_xS_y may follow $\text{Cl}^-/\text{NO}_3^-$ adsorbate scaling relations similar to those of pure metals. In addition, the Rh_xS_y surfaces shown in **Figure 4b** adsorb nitrate very weakly ($\Delta G_{\text{NO}_3^-} > 80 \text{ kJ mol}^{-1}$), thus it is unlikely the pristine Rh_xS_y surfaces are responsible for the NO_3RR activity seen in **Figure 1a**.

Oxygen vacancies catalyze nitrate reduction on TiO_2 and other metal oxide surfaces,⁷¹ and active sites for metal sulfides are often S vacancies^{87,88} or partially reduced surfaces,^{33,87–91} so we investigate S vacancies in Rh_xS_y as possible active sites for NO_3RR . We study S vacancies present on each of the three Rh_xS_y surfaces (**Figure 4c**). Rh_xS_y is known to have partially exposed metal atoms because of sulfur leaching from extended X-ray absorption fine structure in strongly acidic conditions (6 M triflic acid).³³ Though the 1 M H_2SO_4 solution we use to investigate $\text{Rh}_x\text{S}_y/\text{C}$ here is less harsh, we expect a small amount of sulfur leaching from Rh_xS_y to occur. As done for the pristine surfaces, Cl^- , H^+ , and NO_3^- adsorption free energies are calculated on S-defected $\text{Rh}_2\text{S}_3(001)$, $\text{Rh}_3\text{S}_4(100)$, and $\text{Rh}_{17}\text{S}_{15}(100)$. Gibbs adsorption energies of Cl^- and NO_3^- on the three defected surfaces are shown in **Figure 4a** also show linear scaling, indicated by the dotted black line (ΔG_{H} values are included in **Figure S26**). The adsorbate scaling for the S-defected Rh_xS_y is similar to the adsorbate scaling found on the transition metals. Nitrate adsorbs more strongly to S-vacancy sites on Rh_xS_y compared to their pristine surface counterparts. However, the S-vacancy sites also adsorb Cl^- more strongly and would likely be poisoned by chloride. The similar experimental chloride poisoning on $\text{Rh}_x\text{S}_y/\text{C}$ and Rh/C (**Figure 1**) implies that the S-vacancy may be an active site, as those sites follow the nitrate and chloride scaling relation. Because the S-defected $\text{Rh}_3\text{S}_4(100)$ is the surface that has the strongest calculated nitrate adsorption, most similar to $\text{Rh}(211)$, we hypothesize it is the active site, as it would have the highest coverage of nitrate on the surface. However, the rate constant of the surface reaction will also strongly affect the rate and is dictated by the activation energy of the RDS, thus to predict the active site we need to include both of these factors.

We predict the transition state energies for the direct (**Eq. 4**) and H-assisted nitrate dissociation (**Eq. 9**) reactions on pristine and S-defected Rh_xS_y surfaces to estimate the activation energies and rate constants of nitrate reduction and clarify the active site and nitrate dissociation mechanism. The data in **Figure 5** shows the predicted transition state and intermediate energies of nitrate to nitrite on $\text{Rh}_2\text{S}_3(100)$, $\text{Rh}_3\text{S}_4(100)$, and $\text{Rh}_{17}\text{S}_{15}(100)$, both without (**Figures 5a,c**) and with (**Figures 5b,d**) S vacancies. For comparison, the energy profile for direct nitrate reduction to nitrite on $\text{Rh}(211)$ is shown in **Figure 5a**. The geometries are shown in **Figures S14–S17**. The corresponding activation barriers (E_a) are in **Table S6**. For direct reduction, shown in **Figures 5a–b**, all barriers represent a single dissociation step ($\text{NO}_3^* \rightarrow \text{NO}_2^* + \text{O}^*$) and so E_a is just the difference in the energy of the transition state and the adsorbed nitrate. However, for H-assisted reduction in **Figures 5c–d**, a two-step mechanism is possible: hydrogenation of nitrate ($\text{H}^* + \text{NO}_3^* \rightarrow \text{HNO}_3^* + ^*$) followed by dissociation of nitric acid ($\text{HNO}_3^* + ^* \rightarrow \text{NO}_2^* + \text{HO}^*$). For the H-assisted nitrate dissociation, we take the highest barrier for any step on a specific surface as the E_a for the reaction on that surface. For S-defected $\text{Rh}_3\text{S}_4(100)$ and $\text{Rh}_{17}\text{S}_{15}(100)$, barrier calculations did not converge when HNO_3^* was modeled as an intermediate, so the barrier was modeled as a single, combined hydrogenation-dissociation step ($\text{H}^* + \text{NO}_3^* \rightarrow \text{NO}_2^* + \text{HO}^*$) in **Figure 5d**. We were unable to obtain a converged barrier for H-assisted reduction on $\text{Rh}(211)$ after several computational attempts, so only include the direct nitrate dissociation on $\text{Rh}(211)$.

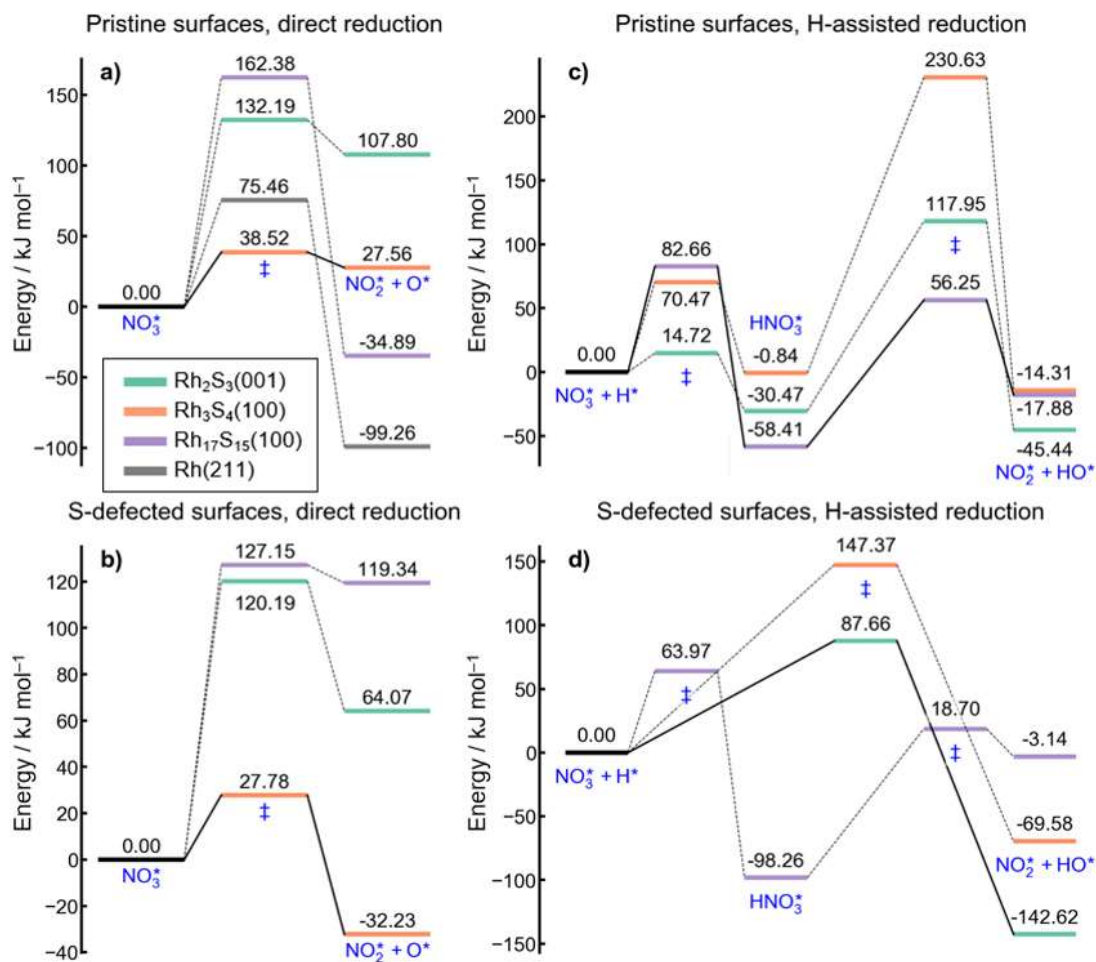


Figure 5. Reaction energy diagram for nitrate to nitrite dissociation on Rh₂S₃(001), Rh₃S₄(100), Rh₁₇S₁₅(100), and Rh(211) surfaces at 0 V vs. SHE. Diagrams are shown for (a, c) pristine versus (b, d) S-defected Rh_xS_y surfaces, and for (a, b) direct nitrate dissociation versus (c, d) H-assisted dissociation. Energies are referenced to the initial state in each diagram, and ‡ refers to a transition state. Color key shown in panel (a): teal = Rh₂S₃(001), orange = Rh₃S₄(100), purple = Rh₁₇S₁₅(100), gray = Rh(211).

With the adsorption energies of hydrogen and nitrate and activation barriers to convert NO₃* to NO₂* calculated on each surface, a theoretical turnover frequency (TOF) can be calculated for each facet and reaction mechanism. The adsorption energies are used to obtain the quasi-equilibrated θ_{NO_3} , θ_{H} , and θ_{H} , as detailed in the ESI. The computed barriers are used to estimate the rate constants k_4 and k_9 in **Eq. 8** and **Eq. 10**, respectively, from an Arrhenius model, where 10^{12} s^{-1} is chosen as a representative pre-exponential factor for all reactions. The parameters input into the microkinetic model are shown in **Table S6**. **Figure 6** shows the computed TOFs for each facet and the two possible mechanisms over the potential range $E = 0$ to 0.4 V vs. RHE.

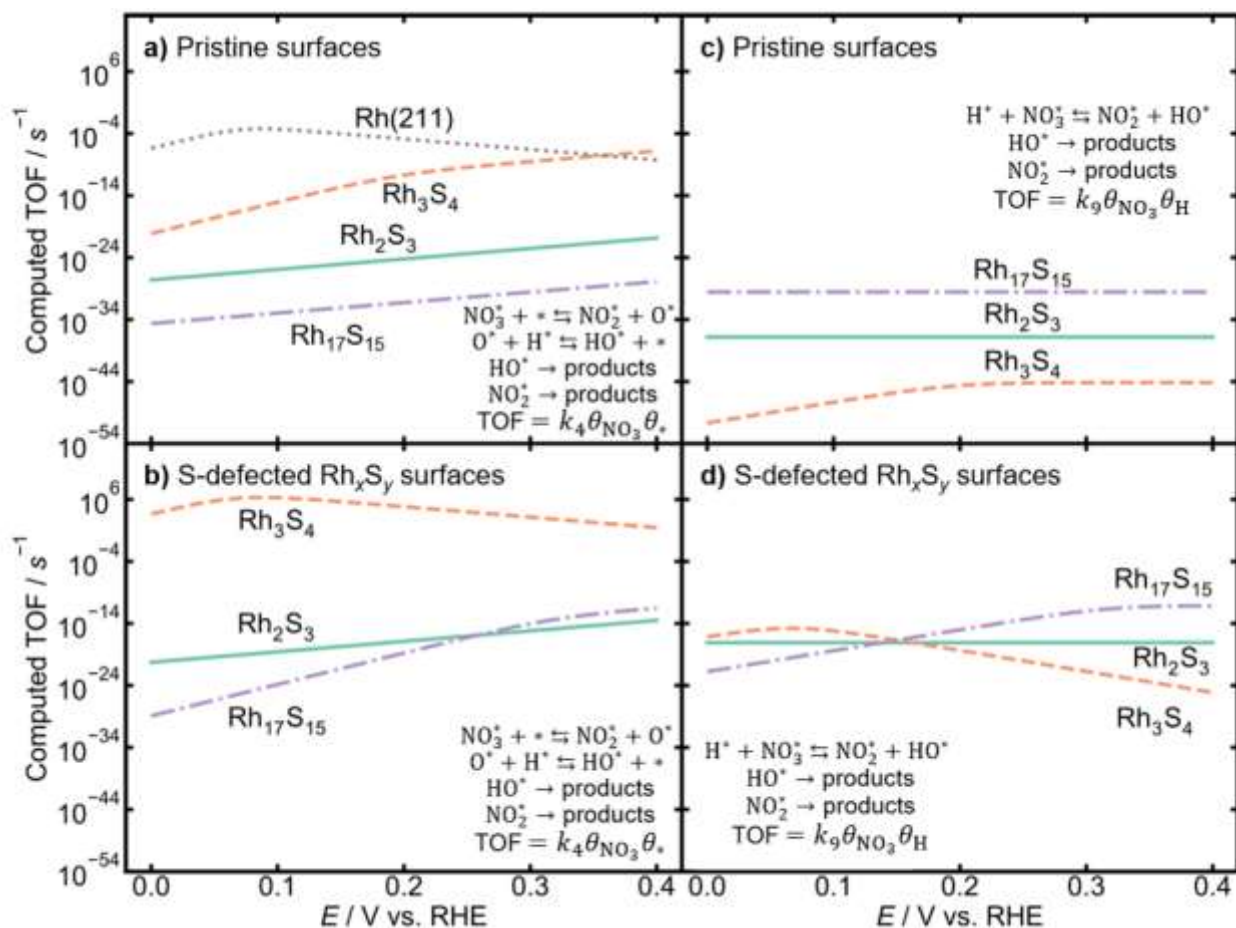


Figure 6. Computed TOFs for nitrate-to-nitrite dissociation as a function of applied potential on $\text{Rh}_2\text{S}_3(001)$, $\text{Rh}_3\text{S}_4(100)$, $\text{Rh}_{17}\text{S}_{15}(100)$, and $\text{Rh}(211)$, with initial solution concentrations of $[\text{NO}_3^-]_0 = [\text{H}^+]_0 = 1 \text{ M}$ and $[\text{Cl}^-]_0 = 0 \text{ M}$. Diagrams are shown for (a, c) pristine versus (b, d) S-defected Rh_xS_y surfaces, and for (a, b) direct nitrate dissociation versus (c, d) H-assisted dissociation. Temperature is 298 K.

The computed TOF curves as a function of applied potential in **Figure 6** predict that S-defected $\text{Rh}_3\text{S}_4(100)$ (**Figure 6b**) has the highest activity and follows the direct nitrate dissociation mechanism. The TOF is higher on the S-defected $\text{Rh}_3\text{S}_4(100)$ facet than on any other sulfide facet, as well as $\text{Rh}(211)$. Although the S-defected $\text{Rh}_3\text{S}_4(100)$ facet is predicted to have the highest activity by the H-assisted mechanism at potentials less than 0.15 V vs. RHE (**Figure 6d**), the absolute TOF through this mechanism is still lower than that of direct nitrate dissociation on the same surface. For applied potentials less than 0.35 V vs. RHE, no pristine surface is more active than $\text{Rh}(211)$ (**Figure 6a**). The high activity of S-defected $\text{Rh}_3\text{S}_4(100)$ is due to its strong nitrate adsorption energy, which enables high coverages of nitrate, and its relatively low activation barrier for nitrate dissociation (**Figure 5b**). S-defected $\text{Rh}_3\text{S}_4(100)$ has a direct nitrate dissociation barrier lower than that of $\text{Rh}(211)$, as well as comparable nitrate and chloride adsorption energies, rationalizing the high activity but moderate chloride poisoning resistance of $\text{Rh}_x\text{S}_y/\text{C}$ observed experimentally (see **Figure S27** for the computational TOFs of S-defected $\text{Rh}_3\text{S}_4(100)$ in the presence of chloride). The experimental observation that $\text{Rh}_x\text{S}_y/\text{C}$ has a higher nitrate reduction current density than Rh/C in 1 M $\text{H}_2\text{SO}_4 + 1 \text{ M NaNO}_3$, but only by a factor of 1.6 to 5.6, is different than the several orders of magnitude shown in **Figure 6**. We attribute this qualitative agreement, but quantitative

disagreement to 1) inaccuracies in our DFT modeling protocol, and 2) the fact that the predicted TOFs in **Figure 6** are for activity per site, and there may in fact be many fewer S-defects in the experimental system compared to non-defected sites, causing the measured TOF to be lower. However, as S-defected $\text{Rh}_3\text{S}_4(100)$ is the most active defect site, and none of the pristine sites are predicted to have high nitrate reduction activity, we attribute the activity of $\text{Rh}_x\text{S}_y/\text{C}$ for nitrate reduction to this site.

Future work to improve the performance of NO_3RR electrocatalysts in the presence of chloride will require verification of the active site and mechanism and preparation of materials with a higher fraction of these active sites. Selecting appropriate synthesis procedures and conditions will promote morphologies containing more such active sites at the surface.⁹² Further testing of the hypothesis that the direct nitrate reduction mechanism is dominant on Rh_xS_y and H-assisted mechanism is dominant on Pt may consist of isotopic labeling studies to identify kinetic isotopic effects. Spectroscopy to determine the active site of Rh_xS_y or to prove the H-assisted mechanism may include electron paramagnetic resonance to detect O- or H-containing radicals,⁹³ which may arise in the hydrogenation of nitrate and the dissociation of HNO_3 . Ultimately, spectroscopy, such as Raman⁴⁰ or X-ray absorption spectroscopy,³³ under NO_3RR conditions is necessary to identify the catalyst structure. Additionally, the activity of the Rh_3S_4 phase can be tested by preparing Rh_xS_y with a higher fraction of Rh_3S_4 and determining whether the NO_3RR activity increases proportionally.^{33,40} Higher catalyst utilization can be achieved by decreasing the particle size⁹⁴ or synthesizing Rh_xS_y catalysts as a shell over a less expensive and more earth-abundant core⁹⁵ to increase the fraction of active sites to total Rh atoms. Based on recent studies of the structure dependence of nitrate reduction,^{73,74} $\text{Rh}_x\text{S}_y/\text{C}$ may be even more active than Rh/C and Pt/C if compared at the same particle size. Future studies of the particle size dependence of nitrate reduction will be needed to confirm or deny this hypothesis. Exploration of site specific competitive adsorption of NO_3^- and Cl^- on Pt may be done using single crystals and deconvolution of the H_{upd} peaks.^{79,80} To decrease the cost of the catalysts, new metal sulfides made of earth-abundant materials may be a useful target.⁹⁶

4. CONCLUSIONS

In this work, we show $\text{Rh}_x\text{S}_y/\text{C}$ is more active for electrocatalytic nitrate reduction than Rh and Pt and has 67% faradaic efficiency towards NH_4^+ at 0.1 V vs. RHE in 0.1 M HNO_3 . When Cl^- is present, however, NO_3RR on $\text{Rh}_x\text{S}_y/\text{C}$ is inhibited only slightly less than Pt/C and Rh/C , in contrast to the highly halide poison resistant behavior of $\text{Rh}_x\text{S}_y/\text{C}$ for reactions such as oxygen reduction and hydrogen evolution. We develop microkinetic models considering direct nitrate dissociation and H-assisted nitrate dissociation to nitrite as the rate-determining step on Pt and Rh and find that H-assisted nitrate dissociation best matches the experimentally observed NO_3RR activity and rate inhibition with chloride for Pt, whereas Rh matches either H-assisted or direct nitrate dissociation. Microkinetic modeling shows that competition between nitrate and chloride for surface coverage greatly influences the nitrate reduction rate. From DFT-calculated adsorption energies and microkinetic modeling, we show that metals that adsorb nitrate strongly and are active for NO_3RR will also adsorb chloride strongly and thus suffer inhibited NO_3RR activity. Rh_3S_4 terraces with S vacancies are predicted to adsorb nitrate strongly and have low activation barriers for direct nitrate dissociation compared to pristine surfaces, resulting in higher activity. S-defected $\text{Rh}_3\text{S}_4(100)$ is predicted to also adsorb chloride strongly and thus exhibit decreased NO_3RR rates, consistent with experimental measurements. Although $\text{Rh}_x\text{S}_y/\text{C}$ is partially inhibited by chloride, it is more resistant to chloride poisoning and more active for NO_3RR than Pt/C or Rh/C . This makes $\text{Rh}_x\text{S}_y/\text{C}$ a suitable catalyst for processes

involving nitrate reduction with chloride present and motivates further studies of S vacancies in metal sulfides for NO₃RR.

CONFLICTS OF INTEREST

The authors declare no competing financial interest.

ACKNOWLEDGMENTS

This work was supported by faculty start-up funds of both Goldsmith and Singh from the University of Michigan, Ann Arbor and a Mcubed seed grant. This research used resources of the National Energy Research Scientific Computing Center (NERSC), a U.S. Department of Energy Office of Science User Facility operated under Contract No. DE-AC02-05CH11231. This work also used the Extreme Science and Engineering Discovery Environment (XSEDE)⁹⁷ *Expanse* supercomputer at the San Diego Supercomputing Center (SDSC) through allocation TG-CHM210001, which is supported by National Science Foundation grant number ACI-1548562. The authors acknowledge James Akinola for help with TEM. The authors acknowledge the University of Michigan College of Engineering and NSF grant #DMR-9871177 for financial support and the Michigan Center for Materials Characterization for staff assistance for TEM.

REFERENCES

- 1 D. E. Canfield, A. N. Glazer and P. G. Falkowski, *Science*, 2010, **330**, 192–196.
- 2 N. Lehnert, H. T. Dong, J. B. Harland, A. P. Hunt and C. J. White, *Nat. Rev. Chem.*, 2018, **2**, 278–289.
- 3 M. Duca and M. T. M. Koper, *Energy Environ. Sci.*, 2012, **5**, 9726–9742.
- 4 M. Ward, R. Jones, J. Brender, T. de Kok, P. Weyer, B. Nolan, C. Villanueva and S. van Breda, *Int. J. Environ. Res. Public Health*, 2018, **15**, 1557.
- 5 N. R. Council, *The Health Effects of Nitrate, Nitrite, and N-Nitroso Compounds*, National Academies Press, Washington, D.C., 1981.
- 6 S. Garcia-Segura, M. Lanzarini-Lopes, K. Hristovski and P. Westerhoff, *Appl. Catal. B Environ.*, 2018, **236**, 546–568.
- 7 N. Singh and B. R. Goldsmith, *ACS Catal.*, 2020, **10**, 3365–3371.
- 8 P. H. van Langevelde, I. Katsounaros and M. T. M. Koper, *Joule*, 2021, **5**, 290–294.
- 9 Z. Wang, D. Richards and N. Singh, *Catal. Sci. Technol.*, 2021, **11**, 705–725.
- 10 Z. Wang, S. D. Young, B. R. Goldsmith and N. Singh, *J. Catal.*, 2021, **395**, 143–154.
- 11 I. Katsounaros, *Curr. Opin. Electrochem.*, 2021, 100721.
- 12 X. Zhang, Y. Wang, C. Liu, Y. Yu, S. Lu and B. Zhang, *Chem. Eng. J.*, 2021, **403**, 126269.
- 13 Y. Wang, C. Wang, M. Li, Y. Yu and B. Zhang, *Chem. Soc. Rev.*, 2021, **50**, 6720–6733.
- 14 Y. Wang, Y. Yu, R. Jia, C. Zhang and B. Zhang, *Natl. Sci. Rev.*, 2019, **6**, 730–738.
- 15 J. Gao, B. Jiang, C. Ni, Y. Qi and X. Bi, *Chem. Eng. J.*, 2020, **382**, 123034.
- 16 Y. Fernández-Nava, E. Marañón, J. Soons and L. Castrillón, *Bioresour. Technol.*, 2008, **99**, 7976–7981.
- 17 R. Chauhan and V. C. Srivastava, *Chem. Eng. J.*, 2020, **386**, 122065.
- 18 A. M. Bergquist, J. K. Choe, T. J. Strathmann and C. J. Werth, *Water Res.*, 2016, **96**, 177–187.

- 19 J. K. Choe, A. M. Bergquist, S. Jeong, J. S. Guest, C. J. Werth and T. J. Strathmann, *Water Res.*, 2015, **80**, 267–280.
- 20 D. Reyter, D. Bélanger and L. Roué, *J. Hazard. Mater.*, 2011, **192**, 507–513.
- 21 D. Reyter, D. Bélanger and L. Roué, *Water Res.*, 2010, **44**, 1918–1926.
- 22 N. Singh, S. Mubeen, J. Lee, H. Metiu, M. Moskovits and E. W. McFarland, *Energy Environ. Sci.*, 2014, **7**, 978–981.
- 23 G. Horányi and E. M. Rizmayer, *J. Electroanal. Chem. Interfacial Electrochem.*, 1982, **140**, 347–366.
- 24 M. Wasberg and G. Horányi, *Electrochim. Acta*, 1995, **40**, 615–623.
- 25 M. Li, C. Feng, Z. Zhang and N. Sugiura, *Electrochim. Acta*, 2009, **54**, 4600–4606.
- 26 D. Pletcher and Z. Poorabedi, *Electrochim. Acta*, 1979, **24**, 1253–1256.
- 27 N. Li and J. Lipkowski, *J. Electroanal. Chem.*, 2000, **491**, 95–102.
- 28 G. Horányi and M. Wasberg, *J. Electroanal. Chem.*, 1996, **404**, 291–298.
- 29 G. Horányi and M. Wasberg, *Electrochim. Acta*, 1997, **42**, 261–265.
- 30 J.-X. Liu, D. Richards, N. Singh and B. R. Goldsmith, *ACS Catal.*, 2019, **9**, 7052–7064.
- 31 F. Gossenberger, T. Roman and A. Groß, *Surf. Sci.*, 2015, **631**, 17–22.
- 32 J. M. Ziegelbauer, D. Gatewood, A. F. Gullá, D. E. Ramaker and S. Mukerjee, *Electrochem. Solid-State Lett.*, 2006, **9**, A430.
- 33 J. M. Ziegelbauer, D. Gatewood, A. F. Gullá, M. J.-F. Guinel, F. Ernst, D. E. Ramaker and S. Mukerjee, *J. Phys. Chem. C*, 2009, **113**, 6955–6968.
- 34 N. Singh, D. C. Upham, R.-F. Liu, J. Burk, N. Economou, S. Buratto, H. Metiu and E. W. McFarland, *Langmuir*, 2014, **30**, 5662–5668.
- 35 J. M. Ziegelbauer, A. F. Gullá, C. O’Laoire, C. Urgeghe, R. J. Allen and S. Mukerjee, *Electrochim. Acta*, 2007, **52**, 6282–6294.
- 36 A. Ivanovskaya, N. Singh, R.-F. Liu, H. Kreutzer, J. Baltrusaitis, T. Van Nguyen, H. Metiu and E. McFarland, *Langmuir*, 2013, **29**, 480–492.
- 37 T. V. Nguyen, H. Kreutzer, V. Yarlagadda, E. McFarland and N. Singh, *ECS Trans.*, 2013, **53**, 75–81.
- 38 J. Masud, J. Walter, T. V. Nguyen, G. Lin, N. Singh, E. McFarland, H. Metiu, M. Ikenberry, K. Hohn, C.-J. Pan and B.-J. Hwang, *ECS Trans.*, 2014, **58**, 37–43.
- 39 J. Masud, T. Van Nguyen, N. Singh, E. McFarland, M. Ikenberry, K. Hohn, C.-J. Pan and B.-J. Hwang, *J. Electrochem. Soc.*, 2015, **162**, F455–F462.
- 40 N. Singh, J. Hiller, H. Metiu and E. McFarland, *Electrochim. Acta*, 2014, **145**, 224–230.
- 41 C. K. Rhee, M. Wasberg, P. Zelenay and A. Wieckowski, *Catal. Letters*, 1991, **10**, 149–164.
- 42 A. Ahmadi, R. W. Evans and G. Attard, *J. Electroanal. Chem.*, 1993, **350**, 279–295.
- 43 G. E. Dima, A. C. A. de Vooy and M. T. M. Koper, *J. Electroanal. Chem.*, 2003, **554–555**, 15–23.
- 44 M. Lukaszewski, M. Soszko and A. Czerwiński, *Int. J. Electrochem. Sci.*, 2016, **11**, 4442–4469.
- 45 J. F. Connolly, R. J. Flannery and G. Aronowitz, *J. Electrochem. Soc.*, 1966, **113**, 577–580.
- 46 N. Singh, M. Gordon, H. Metiu and E. McFarland, *J. Appl. Electrochem.*, 2016, **46**, 497–503.
- 47 B. G. Katz, D. W. Griffin and J. H. Davis, *Sci. Total Environ.*, 2009, **407**, 2872–2886.
- 48 A. D. Eaton, L. S. Clesceri and A. E. (Eds. . Greenberg, *Standard Methods for the Examination of Water and Wastewater*, APHA, New York, NY, 19th Editi., 1995.
- 49 J. M. McEnaney, S. J. Blair, A. C. Nielander, J. A. Schwalbe, D. M. Koshy, M. Cargnello and T. F. Jaramillo, *ACS Sustain. Chem. Eng.*, 2020, **8**, 2672–2681.

- 50 P. Chen, N. Zhang, S. Wang, T. Zhou, Y. Tong, C. Ao, W. Yan, L. Zhang, W. Chu, C. Wu and Y. Xie, *Proc. Natl. Acad. Sci. U. S. A.*, 2019, **116**, 6635–6640.
- 51 G. Kresse and J. Furthmüller, *Phys. Rev. B - Condens. Matter Mater. Phys.*, 1996, **54**, 11169–11186.
- 52 G. Kresse and J. Furthmüller, *Comput. Mater. Sci.*, 1996, **6**, 15–50.
- 53 G. Kresse and J. Hafner, *Phys. Rev. B*, 1994, **49**, 14251–14269.
- 54 G. Kresse and J. Hafner, *Phys. Rev. B*, 1993, **47**, 558–561.
- 55 J. Wellendorff, K. T. Lundgaard, A. Møgelhøj, V. Petzold, D. D. Landis, J. K. Nørskov, T. Bligaard and K. W. Jacobsen, *Phys. Rev. B*, 2012, **85**, 235149.
- 56 S. Mallikarjun Sharada, R. K. B. Karlsson, Y. Maimaiti, J. Voss and T. Bligaard, *Phys. Rev. B*, 2019, **100**, 035439.
- 57 D. Joubert, *Phys. Rev. B - Condens. Matter Mater. Phys.*, 1999, **59**, 1758–1775.
- 58 P. E. Blöchl, *Phys. Rev. B*, 1994, **50**, 17953–17979.
- 59 P. Wisesa, K. A. McGill and T. Mueller, *Phys. Rev. B*, 2016, **93**, 155109.
- 60 F. Calle-Vallejo, M. Huang, J. B. Henry, M. T. M. Koper and A. S. Bandarenka, *Phys. Chem. Chem. Phys.*, 2013, **15**, 3196.
- 61 S. Taguchi and J. M. Feliu, *Electrochim. Acta*, 2007, **52**, 6023–6033.
- 62 G. Henkelman, B. P. Uberuaga and H. Jónsson, *J. Chem. Phys.*, 2000, **113**, 9901–9904.
- 63 G. Henkelman and H. Jónsson, *J. Chem. Phys.*, 1999, **111**, 7010–7022.
- 64 A. Heyden, A. T. Bell and F. J. Keil, *J. Chem. Phys.*, 2005, **123**, 224101.
- 65 K. T. Jacob and P. Gupta, *J. Chem. Thermodyn.*, 2014, **70**, 39–45.
- 66 O. Diéguez and N. Marzari, *Phys. Rev. B*, 2009, **80**, 214115.
- 67 S. P. Ong, W. D. Richards, A. Jain, G. Hautier, M. Kocher, S. Cholia, D. Gunter, V. L. Chevrier, K. A. Persson and G. Ceder, *Comput. Mater. Sci.*, 2013, **68**, 314–319.
- 68 J. H. Montoya and K. A. Persson, *npj Comput. Mater.*, 2017, **3**, 14.
- 69 L. Wei, D. J. Liu, B. A. Rosales, J. W. Evans and J. Vela, *ACS Catal.*, 2020, **10**, 3618–3628.
- 70 W. Siriwatcharapiboon, Y. Kwon, J. Yang, R. L. Chantry, Z. Li, S. L. Horswell and M. T. M. Koper, *ChemElectroChem*, 2014, **1**, 172–179.
- 71 R. Jia, Y. Wang, C. Wang, Y. Ling, Y. Yu and B. Zhang, *ACS Catal.*, 2020, **10**, 3533–3540.
- 72 H. Liu, J. Park, Y. Chen, Y. Qiu, Y. Cheng, K. Srivastava, S. Gu, B. H. Shanks, L. T. Roling and W. Li, *ACS Catal.*, 2021, **2**, 8431–8442.
- 73 J. Lim, C.-Y. Liu, J. Park, Y. Liu, T. P. Senftle, S. W. Lee and M. C. Hatzell, *ACS Catal.*, 2021, **11**, 7568–7577.
- 74 Y. Han, X. Zhang, W. Cai, H. Zhao, Y. Zhang, Y. Sun, Z. Hu, S. Li, J. Lai and L. Wang, *J. Colloid Interface Sci.*, 2021, **600**, 620–628.
- 75 O. Brylev, M. Sarrazin, L. Roué and D. Bélanger, *Electrochim. Acta*, 2007, **52**, 6237–6247.
- 76 Y. Guo, X. Cai, S. Shen, G. Wang and J. Zhang, *J. Catal.*, 2021, **402**, 1–9.
- 77 G. Jerkiewicz, *Electrocatalysis*, 2010, **1**, 179–199.
- 78 B. Łosiewicz, R. Jurczakowski and A. Lasia, *Electrochim. Acta*, 2011, **56**, 5746–5753.
- 79 I. T. McCrum and M. J. Janik, *J. Phys. Chem. C*, 2017, **121**, 6237–6245.
- 80 I. T. McCrum and M. J. Janik, *J. Phys. Chem. C*, 2016, **120**, 457–471.
- 81 R. Gómez, J. M. Orts, B. Álvarez-Ruiz and J. M. Feliu, *J. Phys. Chem. B*, 2004, **108**, 228–238.
- 82 Y. Ishikawa, J. J. Mateo, D. A. Tryk and C. R. Cabrera, *J. Electroanal. Chem.*, 2007, **607**, 37–46.
- 83 V. Stamenkovic, N. M. Markovic and P. N. Ross, *J. Electroanal. Chem.*, 2001, **500**, 44–51.

- 84 N. Markovic, M. Hanson, G. McDougall and E. Yeager, *J. Electroanal. Chem. Interfacial Electrochem.*, 1986, **214**, 555–566.
- 85 K. Mathew, R. Sundararaman, K. Letchworth-Weaver, T. A. Arias and R. G. Hennig, *J. Chem. Phys.*, 2014, **140**, 084106.
- 86 Z.-J. Zhao, S. Liu, S. Zha, D. Cheng, F. Studt, G. Henkelman and J. Gong, *Nat. Rev. Mater.*, 2019, **4**, 792–804.
- 87 Z. He, Y. Wang, X. Dong, N. Zheng, H. Ma and X. Zhang, *RSC Adv.*, 2019, **9**, 21646–21652.
- 88 S. Hu, X. Chen, Q. Li, Y. Zhao and W. Mao, *Catal. Sci. Technol.*, 2016, **6**, 5884–5890.
- 89 L. Wang, S. Guo, Y. Chen, M. Pan, E. H. Ang and Z. Yuan, *ChemPhotoChem*, 2020, **4**, 110–119.
- 90 E. J. M. Hensen, M. J. Vissenberg, V. H. J. de Beer, J. A. R. van Veen and R. A. van Santen, *J. Catal.*, 1996, **163**, 429–435.
- 91 R. C. Brunet and L. J. Garcia-Gil, *FEMS Microbiol. Ecol.*, 1996, **21**, 131–138.
- 92 M. A. Ehsan, A. Adam, A. Rehman, A. S. Hakeem, A. A. Isab and M. Qamar, *Sustain. Energy Fuels*, 2021, **5**, 459–468.
- 93 N. Senesi and G. S. Senesi, in *Encyclopedia of Soils in the Environment*, Elsevier, 2005, pp. 426–437.
- 94 Y. Li and T. Van Nguyen, *Energies*, 2020, **13**, 3971.
- 95 Y. Li and T. Van Nguyen, *J. Power Sources*, 2018, **382**, 152–159.
- 96 A. S. Fajardo, P. Westerhoff, C. M. Sanchez-Sanchez and S. Garcia-Segura, *Appl. Catal. B Environ.*, 2021, **281**, 119465.
- 97 J. Towns, T. Cockerill, M. Dahan, I. Foster, K. Gaither, A. Grimshaw, V. Hazlewood, S. Lathrop, D. Lifka, G. D. Peterson, R. Roskies, J. R. Scott and N. Wilkins-Diehr, *Comput. Sci. Eng.*, 2014, **16**, 62–74.